Spin Torque–Generated Magnetic Droplet Solitons

S. M. Mohseni *et al.*
Science **339**, 1295 (2013);
DOI: 10.1126/science.1230155

Spin Torque–Generated Magnetic Droplet Solitons

S. M. Mohseni,[1,2] S. R. Sani,[1,2] J. Persson,[2] T. N. Anh Nguyen,[1] S. Chung,[1,3] Ye. Pogoryelov,[3] P. K. Muduli,[3,4] E. Iacocca,[3] A. Eklund,[5] R. K. Dumas,[3] S. Bonetti,[1,6] A. Deac,[7] M. A. Hoefer,[8] J. Åkerman[1,2,3]*

Dissipative solitons have been reported in a wide range of nonlinear systems, but the observation of their magnetic analog has been experimentally challenging. Using spin transfer torque underneath a nanocontact on a magnetic thin film with perpendicular magnetic anisotropy (PMA), we have observed the generation of dissipative magnetic droplet solitons and report on their rich dynamical properties. Micromagnetic simulations identify a wide range of automodulation frequencies, including droplet oscillatory motion, droplet "spinning," and droplet "breather" states. The droplet can be controlled by using both current and magnetic fields and is expected to have applications in spintronics, magnonics, and PMA-based domain-wall devices.

Dissipative solitons are localized excitations realized by a balance between nonlinearity, dispersion, gain, and loss (1, 2). They can be experimentally observed in optical (3, 4), chemical (5, 6), granular (7), and liquid (8) dissipative systems. Large amplitude nanoscale dynamics in magnetic thin films with perpendicular magnetic anisotropy (PMA) inherently possess all mechanisms supporting dissipative solitons except for gain. Spin-transfer torque (STT) (9–12) provides for the injection of angular momentum from spin-polarized electrons into a magnet. Using STT as the gain mechanism in nanocontact (NC)–based spin-torque oscillators (STOs), a magnetic dissipative soliton—the so-called "magnetic droplet"—was recently proposed (13–15). Using NC-STOs, we created and investigated magnetic droplet dynamics experimentally.

Classical conservative solitons, such as light pulses in a virtually lossless optical fiber, preserve their shape by balancing the opposing effects of dispersion (spreading) and nonlinearity (focusing). Similarly, if damping is ignored the Landau-Lifshitz equation for an extended two-dimensional magnetic thin film with PMA can sustain a family of conservative magnetic solitons, known as "magnon drops" (16, 17). All spins in a magnon drop precess in phase around the film normal, with a precession angle $0 < \Theta(0) < \pi$ at the center of the drop and $0 < \Theta(r) < \Theta(0)$ decreasing exponentially fast, with radius to 0 in the far field. The family of stationary magnon drops can be parameterized by the precessional frequency f_0, satisfying $f_{Zeeman} < f_0 < f_{FMR}$, where f_{FMR} is the ferromagnetic resonance (FMR) frequency, and f_{Zeeman} is the Zeeman frequency. Magnon drops can be strongly nonlinear, exhibiting almost fully reversed cores [$\Theta(0) \to \pi$] for f_0 close to f_{Zeeman}. Whereas conservative magnon drops balance exchange (dispersion) with anisotropy (nonlinearity) for each f_0, the dissipative magnetic droplet must also balance energy gain (STT) with dissipation (damping), singling out a particular droplet precession frequency for a given drive current and applied field (Fig. 1C) (13). More generally, dissipative soliton systems, such as the NC-STOs studied here, are natural environments for studying pattern formation. Dissipative solitons are often robust attractors and can exhibit exotic dynamics, such as time-periodic breathing (1). It has been claimed that NC-STOs with in-plane anisotropy and applied field exhibit nonlinear localization in the form of a weakly nonlinear spin wave bullet with precession angles much less than 90° (18, 19). In contrast, the fully nonlinear dissipative droplet studied here neces-

sarily involves precession angles greater than 90° (13), exhibiting a clear experimental signature and rich nonlinear behavior.

To test the theoretical predictions for a magnetic droplet (13), we fabricated NC-STOs based on orthogonal pseudospin valve stacks (Fig. 1C), in which the magnetization of the Co fixed layer lies in the plane for zero applied field, whereas that of the Co/Ni multilayer free layer lies along the film normal because PMA is sufficiently strong to overcome the demagnetization field (20–22).

The field dependence of the microwave signal from a NC-STO with 63-nm NC diameter in low to moderate perpendicular fields (Fig. 1A) shows the expected linear FMR-like field dependence (20, 21). However, at a critical field of $\mu_0 H_{droplet} = 0.65$ T, the precession frequency exhibits a dramatic drop to a frequency that lies between the Zeeman and FMR frequencies, with a simultaneous jump in the integrated power (P). A similarly dramatic transition can be observed (Fig. 1B) as a function of current in a constant field of 0.8 T with similar changes in frequency and power. To gain further insight into the magnetic state as a function of field and current, the magnetoresistance {MR = [$R(H) - R(H = 0)$]/$R(H = 0)$, where R is the device resistance} was measured both at –6 mA and at a lower current of –1 mA (Fig. 1A, inset). Below 0.65 T, the MR exhibits an identical linear decrease for both currents, which is consistent with a linearly increasing out-of-plane component of the fixed layer magnetization and an increasingly parallel state of the NC-STO. At exactly $\mu_0 H_{droplet} = 0.65$ T, MR [current (I) = –6 mA] exhibits a jump of 0.1%, and its field dependence changes sign; the NC-STO state thus becomes increasingly antiparallel with increasing field. Contrarily, MR (I = –1 mA) does not show any sign of transition and continues to decrease linearly, eventually saturating in a field of 1.6 to 1.8 T (fig. S1) (22), which is consistent with the expected saturation field for the Co layer.

Both the dynamic and static observations are consistent with the formation of a magnetic droplet in the free layer. The large drop in frequency and the sign change of the field-dependent resistance further indicate a substantially reversed central region. This is corroborated by the large increase in microwave power because a reversed droplet will have a large area of spins precessing around the equator, whereas the precession angle of the FMR-like mode is very limited close to the threshold for STO dynamics (10, 13). Last, according to the theory of the magnetic droplet, its

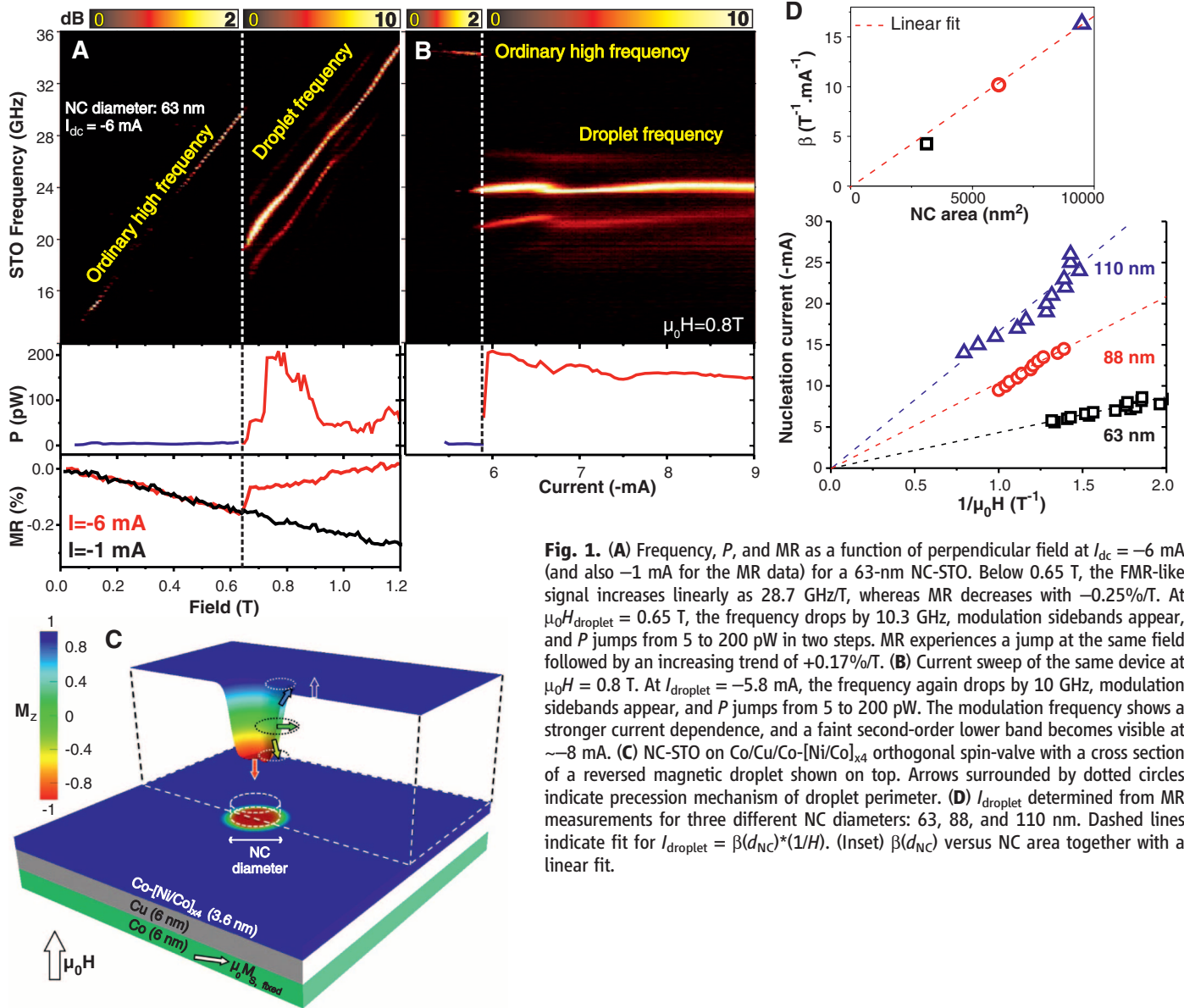**Fig. 1.** (**A**) Frequency, *P*, and MR as a function of perpendicular field at $I_{dc} = -6$ mA (and also −1 mA for the MR data) for a 63-nm NC-STO. Below 0.65 T, the FMR-like signal increases linearly as 28.7 GHz/T, whereas MR decreases with −0.25%/T. At $\mu_0 H_{droplet} = 0.65$ T, the frequency drops by 10.3 GHz, modulation sidebands appear, and *P* jumps from 5 to 200 pW in two steps. MR experiences a jump at the same field followed by an increasing trend of +0.17%/T. (**B**) Current sweep of the same device at $\mu_0 H = 0.8$ T. At $I_{droplet} = -5.8$ mA, the frequency again drops by 10 GHz, modulation sidebands appear, and *P* jumps from 5 to 200 pW. The modulation frequency shows a stronger current dependence, and a faint second-order lower band becomes visible at ~−8 mA. (**C**) NC-STO on Co/Cu/Co-[Ni/Co]$_{x4}$ orthogonal spin-valve with a cross section of a reversed magnetic droplet shown on top. Arrows surrounded by dotted circles indicate precession mechanism of droplet perimeter. (**D**) $I_{droplet}$ determined from MR measurements for three different NC diameters: 63, 88, and 110 nm. Dashed lines indicate fit for $I_{droplet} = \beta(d_{NC})*(1/H)$. (Inset) $\beta(d_{NC})$ versus NC area together with a linear fit.

frequency ($f_{droplet}$) should increase linearly with field at a slope of $\gamma/2\pi$ (γ is the gyromagnetic ratio, so $\gamma/2\pi = 28.7$ GHz/T) and decrease very weakly with current, which is in agreement with Fig. 1, A and B, respectively.

From the MR value at the transition, we can conclude that the Co layer tilt angle required to nucleate a droplet at –6 mA is ~50°. Assuming that the nucleation is primarily driven by the perpendicular component of the spin-polarized current density, we expect the required nucleation current to be inversely proportional to the perpendicular component M_z of the fixed layer magnetization. Because M_z is linearly proportional to the perpendicular field for the easy-plane Co (fig. S1) (*22*), we can directly test this assumption by plotting the nucleation current ($I_{droplet}$) versus inverse applied field, $1/H$ (Fig. 1D). We indeed observed that $I_{droplet}$ is inversely proportional to the applied field and that the slope of this depen-

dence scales with NC area, confirming that the droplet nucleation is governed by the perpendicular component of the spin-polarized current density, regardless of the applied field and NC size.

We now turn to the modulation sidebands that appear simultaneously with the nucleation of the magnetic droplet. The droplet and its field dependence are very robust and reproducible from device to device; however, we found greater variation in the modulation, with some devices showing single (Fig. 2A) and multiple (Fig. 2B) well-defined sideband pairs, some showing strong peaks at $f_{droplet}/2$ (with some power at $3f_{droplet}/2$) (Fig. 2C) and others not showing any modulation at any current or field. In some cases, pure single-tone operation may be preceded by modulated behavior at lower currents (Fig. 2B); the onset current is dependent on the direction of the current sweep. The low-frequency (~1 GHz) modulating signal can be measured directly (Fig. 2A).

Because all of our measurements involved dc drive alone, the observed modulation is unrelated to ordinary STO modulation (*23*, *24*), in which the drive current contains an intentionally superimposed modulating current. The observed automodulation must instead be intrinsic to the droplet.

With the aid of dissipative droplet theory and micromagnetic simulations (*22*), we can identify these complex dynamics with different dynamical wave states, including quasiperiodic and periodic structures. At nucleation, the dramatic drop in frequency is associated with droplet formation (*13*), in which all the spins in the droplet precess uniformly at a single fixed frequency (Fig. 3A). In (*13*), a droplet drift instability was identified when the droplet was ejected from the NC area, eventually succumbing to damping, leaving room for the nucleation of a new droplet in a periodic fashion. This process occurs on a nanosecond time scale, which is consistent with
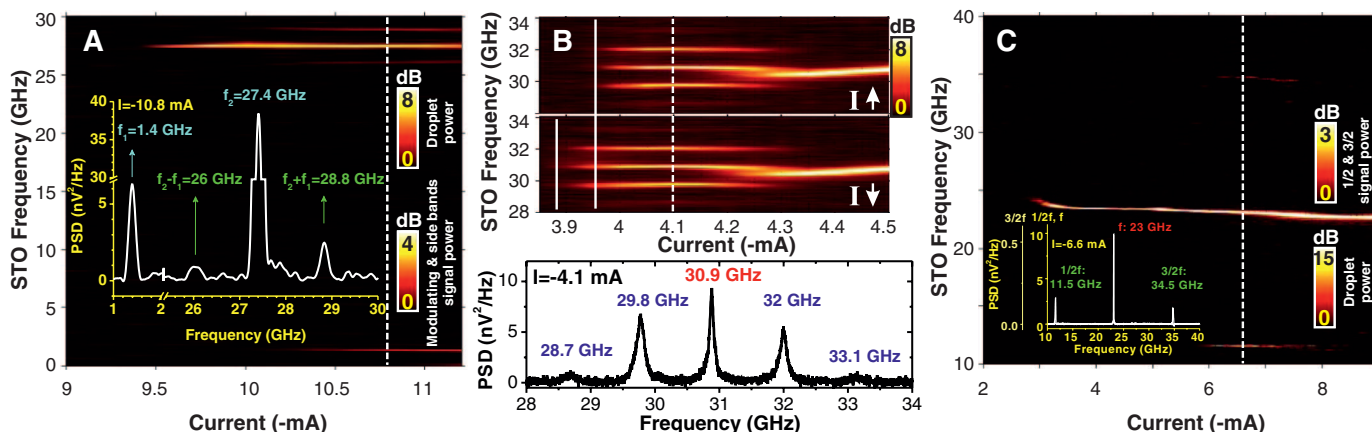
Fig. 2. (A) Droplet automodulation in an 88-nm NC-STO (perpendicular field of 0.9 T). (Inset) Power spectral density (PSD) at −10.8 mA showing both the modulating signal at 1.4 GHz and the resulting modulation sidebands. **(B)** Automodulation in a 60-nm NC-STO (perpendicular field of 0.9 T) leading to both first- and second-order sidebands (PSD at −4.1 mA shown in the inset below). The onset current (solid white lines) exhibit a hysteresis of ~0.1 mA. **(C)** Observation of sidebands at $f_{droplet}/2$ and $3f_{droplet}/2$ (63-nm NC-STO, 0.8-T field applied at 30° to the plane), which is consistent with droplet breathing. (Inset) PSD at −6.6 mA. Shown is the different scale for the much weaker sideband signals.
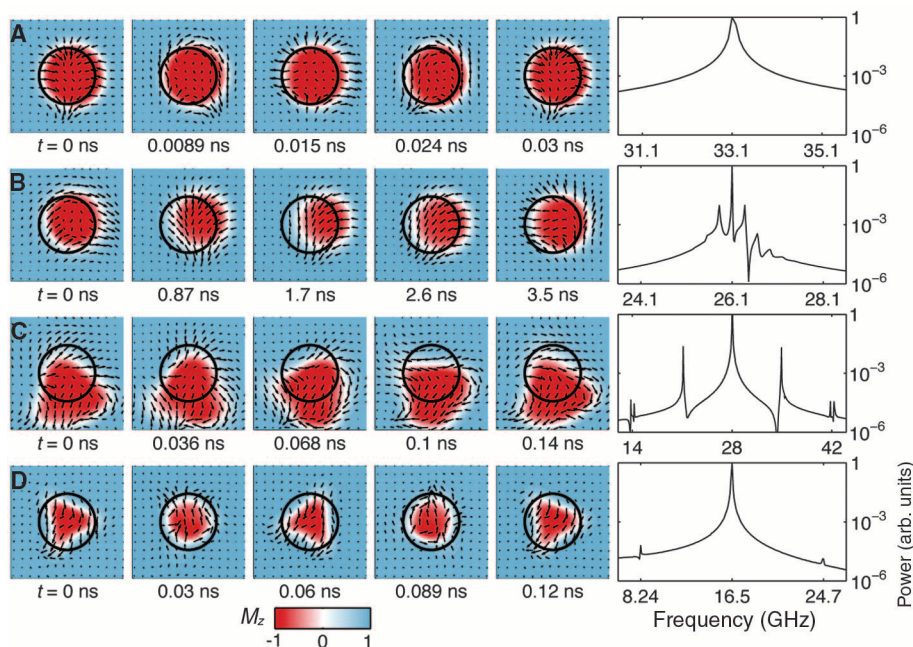

Fig. 3. Time sequences of out-of-plane, M_z (in color), and in-plane (vector field) magnetization component of free layer from micromagnetic simulation. (Right) The power spectrum associated with the NC-averaged projection of magnetization onto the polarization layer. Parameters are given as triples (field, NC diameter, and current). **(A)** Stationary droplet precession with a single spectral peak for large field (1.1 T, 80 nm, and −12 mA). **(B)** Droplet oscillation leading to prominent sidebands for moderate field (0.8 T, 63 nm, and −8 mA). **(C)** Spinning of an asymmetric droplet for moderate field (0.9 T, 50 nm, and −9 mA). **(D)** Droplet perimeter deformations (breathing) with period twice the precessional period (0.5 T, 80 nm, and −8 mA).

the experimentally observed modulation sidebands. However, this explanation is not consistent with the observed hysteresis (Fig. 2B), predicted for stable, nondrifting droplets (13), because it precludes the periodic death and rebirth of the droplet. Upon decrease of the current below the nucleation threshold, a new droplet cannot form once the first droplet has disappeared. Micromagnetic simulations reveal two possible explanations for this discrepancy relying on the presence of a sufficiently canted polarizer for moderate fields. The drifting droplet may experience a restoring force leading to gyrotropic-like motion of the droplet within the NC area with a characteristic ~1 GHz frequency (Fig. 3B); depending on other parameters, micromagnetic simulations also reveal asymmetric droplets that "spin" on the edge of the NC area

while emitting spin waves (Fig. 3C), exhibiting sidebands with frequency spacings of several GHz. For strong canting of the polarizer away from the film normal (weak fields), we observed periodic dynamics with signals at 1/2 and 3/2 of the fundamental frequency (Fig. 3D). We identify these characteristic signals with a breathing mode whose observed breathing frequency is half the precessional frequency (Fig. 2C). Generally, micromagnetic simulations at larger fields tend to exhibit stable precessional dynamics, whereas lower fields can lead to unstable behavior or modulation sidebands by way of droplet oscillations, breathing, and spinning.

Besides the fundamental interest of the creation and control of dissipative solitons in magnetic systems—including, for example, surface magnetic drops expected in thick PMA films (25)—the observed magnetic droplet may have an impact on applications, in particular its influence on the emerging fields of STOs, domain-wall electronics, and magnonics. For STOs, the dramatic frequency drop enables ultra-broadband frequency-shift keying (26), in which the carrier frequency can be switched by ~10 GHz by varying the drive current a fraction of its absolute value. Micromagnetic simulations indicate nucleation on the sub-nanosecond time scale, but the definitive modulation rate should be determined experimentally. In the emerging field of domain-wall electronics with PMA materials (27), the magnetic droplet may be used as a current-controlled nanoscopic domain-wall injector and hence facilitate the implementation of compact domain-wall devices. By applying local field gradients, the magnetic droplet can be transported away from the nanocontact region (14, 15), carrying information on its own or spatially modifying local spin wave propagation in magnonic devices (28–30). These magnetic droplets hence may join domain walls and magnetic vortices as distinct and useful nanomagnetic objects.

References and Notes

1. N. N. Akhmediev, A. Ankiewicz, *Lect. Notes Phys.* **751**, 1 (2008).
2. N. J. Zabusky, M. D. Kruskal, *Phys. Rev. Lett.* **15**, 240 (1965).
3. V. B. Tarananko, K. Staliunas, C. O. Weiss, *Phys. Rev. Lett.* **81**, 2236 (1998).
4. S. Barland *et al.*, *Nature* **419**, 699 (2002).
5. S. L. Lane, D. Luss, *Phys. Rev. Lett.* **70**, 830 (1993).
6. H. H. Rotermund, S. Jakubith, G. Ertl, G. Ertl, A. von Oertzen, *Phys. Rev. Lett.* **66**, 3083 (1991).
7. P. B. Umbanhowar, F. Melo, H. L. Swinney, *Nature* **382**, 793 (1996).
8. F. Melo, S. Douady, *Phys. Rev. Lett.* **71**, 3283 (1993).
9. J. C. Slonczewski, *J. Magn. Magn. Mater.* **159**, L1 (1996).
10. J. C. Slonczewski, *J. Magn. Magn. Mater.* **195**, L261 (1999).
11. L. Berger, *Phys. Rev. B* **54**, 9353 (1996).
12. D. Ralph, M. Stiles, *J. Magn. Magn. Mater.* **320**, 1190 (2008).
13. M. A. Hoefer, T. J. Silva, M. W. Keller, *Phys. Rev. B* **82**, 054432 (2010).
14. M. A. Hoefer, M. Sommacal, *Physica D* **241**, 890 (2012).
15. M. A. Hoefer, M. Sommacal, T. J. Silva, *Phys. Rev. B* **85**, 214433 (2012).
16. B. A. Ivanov, A. M. Kosevich, *Zh. Eksp. Teor. Fiz.* **72**, 2000 (1977).
17. A. M. Kosevich, B. A. Ivanov, A. S. Kovalev, *Phys. Rep.* **194**, 117 (1990).
18. A. Slavin, V. Tiberkevich, *Phys. Rev. Lett.* **95**, 237201 (2005).
19. S. Bonetti *et al.*, *Phys. Rev. Lett.* **105**, 217204 (2010).
20. W. H. Rippard *et al.*, *Phys. Rev. B* **81**, 014426 (2010).
21. S. M. Mohseni *et al.*, *Phys. Status Solidi RRL* **5**, 432 (2011).
22. Materials and methods are available as supplementary materials on *Science* Online.
23. M. R. Pufall, W. H. Rippard, S. Kaka, T. J. Silva, S. E. Russek, *Appl. Phys. Lett.* **86**, 082506 (2005).
24. P. K. Muduli *et al.*, *Phys. Rev. B* **81**, 140408(R) (2010).
25. Yu. I. Bespyatykh, I. E. Dikshtein, S. A. Nikitov, *Phys. Lett. A* **184**, 198 (1994).
26. M. Manfrini *et al.*, *Appl. Phys. Lett.* **95**, 192507 (2009).
27. O. Boulle, G. Malinowski, M. Kläui, *Mater. Sci. Eng. Rep.* **72**, 159 (2011).
28. V. V. Kruglyak, S. O. Demokritov, D. Grundler, *J. Phys. D Appl. Phys.* **43**, 264001 (2010).
29. V. E. Demidov, S. Urazhdin, S. O. Demokritov, *Nat. Mater.* **9**, 984 (2010).
30. M. Madami *et al.*, *Nat. Nanotechnol.* **6**, 635 (2011).

Flexible Minerals: Self-Assembled Calcite Spicules with Extreme Bending Strength

Filipe Natalio,[1,2] Tomas P. Corrales,[3] Martin Panthöfer,[1] Dieter Schollmeyer,[4] Ingo Lieberwirth,[3] Werner E. G. Müller,[5] Michael Kappl,[3] Hans-Jürgen Butt,[3] Wolfgang Tremel[1]*

Silicatein-α is responsible for the biomineralization of silicates in sponges. We used silicatein-α to guide the self-assembly of calcite "spicules" similar to the spicules of the calcareous sponge *Sycon* sp. The self-assembled spicules, 10 to 300 micrometers (μm) in length and 5 to 10 μm in diameter, are composed of aligned calcite nanocrystals. The spicules are initially amorphous but transform into calcite within months, exhibiting unusual growth along [100]. They scatter x-rays like twinned calcite crystals. Whereas natural spicules evidence brittle failure, the synthetic spicules show an elastic response, which greatly enhances bending strength. This remarkable feature is linked to a high protein content. With nano-thermogravimetric analysis, we measured the organic content of a single spicule to be 10 to 16%. In addition, the spicules exhibit waveguiding properties even when they are bent.

The organisms of various phyla have developed complex and intriguing strategies to deposit minerals in their structural frameworks. Most of them are directed by organic matrices, which control size, shape, organization, and even the mineral phase (*1*–*3*). A simple biological design strategy is to use single crystals. Amorphous precursors (*4*–*7*) are used to mold biominerals into their final forms (*6*–*8*) and to prevent unintentional calcification by rapid precipitation. (*5*) Organic macromolecules have been shown to play a pivotal role. They stabilize the transient phases (*9*, *10*), influence the shape, and overcome the intrinsic brittleness of the crystalline phase (*11*). Macromolecules create defects in the lattice, which strengthen the crystal against fracture by absorbing stress and stopping the propagation of cracks (*12*). Occluded macromolecules are—at least in part—responsible for the shape of biominerals by inhibiting their growth in certain directions. In addition, the observed anisotropic distribution of defects indicates that the macromolecules are arranged in certain crystal directions (*3*, *12*). An early structural study of calcitic sponge spicules revealed a morphological and textural symmetry different from the hexagonal symmetry of calcite, indicating an additional level of biological control (*13*).

The intricate structures observed in biominerals have inspired the development of synthetic strategies to mimic nature. The precipitation of minerals in the presence of soluble organic additives has proven to be highly successful in the regulation of crystal morphology and nanostructures (*14*). Although nature produces sophisticated structures with remarkable ease and fidelity, the synthesis of their artificial counterparts is still a challenge. The fabrication of materials that resemble spicules—calcareous or siliceous—is even more difficult because it involves dissimilar organic and inorganic nanophases. The principle of controlled nucleation occurs in both siliceous (noncrystalline) and calcareous (crystalline) biomineralization independently of their chemical nature.

One important protein responsible for the formation of siliceous spicules in sponges is silicatein-α. This ~23-kD protein, which has been shown to form oligomers and fibrous structures through self-aggregation (*15*), catalyzes and structurally directs the formation of silica spicules. (*16*) Here, we demonstrate that silicatein-α can also be used to form synthetic spicules of calcium carbonate. The mechanical properties of the synthetic spicules proved to be superior to those of biogenic material. For comparison, we used the spicules (monoaxa) of the calcareous sponge *Sycon* sp. (*Porifera*, *Calcarea*) (*12*, *13*), which are morphologically very similar to our synthetic calcite spicules.

A solution of freshly prepared $CaCl_2$ (5 mM) was mixed on a cleaned mica surface with refolded recombinant silicatein-α (210 μg/mL, pH 7.4). This was then exposed to CO_2 partial pressure above solid ammonium carbonate [$(NH_4)_2CO_3$] for 4 hours at room temperature (RT) in a sealed desiccator (*17*). Needle-like crystals ("synthetic spicules") with smooth surfaces, diameters of 5 to 10 μm, and lengths of 10 to 300 μm were formed (Fig. 1, A and B). A scanning electron microscopy (SEM) image (Fig. 1B, inset) of a cross section of a synthetic spicule prepared by use of a focused ion beam (FIB) revealed a uniform, homogeneous, and circular structure. In the absence of silicatein-α, only rhombohedral calcite crystals were formed (fig. S1A).

The presence of silicatein-α is evident from the Fourier transform infrared (FT-IR) spectrum

[1]Institut für Anorganische Chemie und Analytische Chemie, Johannes Gutenberg-Universität, Duesbergweg 10-14, D-55099 Mainz, Germany. [2]Institut für Chemie–Anorganische Chemie, Martin-Luther-Universität Halle-Wittenberg, Kurt Mothes Straβe 2, 06120 Halle, Germany. [3]Max-Planck-Institut für Polymerforschung, Ackermannweg 10, D-55128 Mainz, Germany. [4]Institut für Organische Chemie, Johannes Gutenberg-Universität, Duesbergweg 10-14, D-55099 Mainz, Germany. [5]Institut für Physiologische Chemie, Universitätsmedizin, Johannes Gutenberg-Universität, Duesbergweg 6, D-55099 Mainz, Germany.

*To whom correspondence should be addressed. E-mail: tremel@uni-mainz.de